Trajectory Envelope of a Subsea Shuttle Tanker Hovering in Stochastic Ocean Current - Model Development and Tuning

Yucong Ma, first author[1]
Department of Mechanical and Structural Engineering and Materials Science, University of Stavanger
Kjell Arholms gate 41, 4021 Stavanger
yucong.ma@uis.no

Yihan Xing, second author
Department of Mechanical and Structural Engineering and Materials Science, University of Stavanger
Kjell Arholms gate 41, 4021 Stavanger
yihan.xing@uis.no

Dan Sui, third author
Department of Energy and Petroleum Engineering, University of Stavanger
Kjell Arholms gate 41, 4021 Stavanger
dan.sui@uis.no

[1] yucong.ma@uis.no

ABSTRACT

A subsea shuttle tanker (SST) concept for liquid carbon dioxide transportation was recently proposed to support studies evaluating the ultra-efficient underwater cargo submarine concept. One important topic is the position keeping ability of SST during the offloading process. In this process, the SST hovers above the well and connects with the wellhead using a flowline. This process takes around four hours. Ocean currents can cause tremendous drag forces on the subsea shuttle tanker during this period. The flow velocities over hydroplanes are low throughout this process, and the generated lift forces are generally insufficient to maintain the SST's depth. The ballast tanks cannot provide such fast actuation to cope with the fluctuation of the current. It is envisioned that tunnel thrusters that can provide higher frequency actuation are required. This paper develops a manoeuvring model and designs a linear quadratic regulator that facilitates the SST station-keeping problem in stochastic current. As case studies, the SST footprints at 0.5 m/s, 1.0 m/s, and 1.5 m/s mean current speeds are presented. Numerical results show that the designed hovering control system can ensure the SST's stationary during offloading. The required thrust from thrusters and the propeller are presented. The presented model can serve as a basis for obtaining a more efficient design of the SST and provide recommendations for the SST operation.

Keywords: subsea shuttle tanker, autonomous underwater vehicle, submarine, hovering, linear quadratic regulator, subsea technology

1 INTRODUCTION

1.1 Subsea Shuttle Tanker

Offshore oil and gas products are commonly transported by submarine pipelines or tanker ships from fields to onshore facilities [1]. Submarine pipelaying has accumulated a significant amount of knowledge and experience since it was first developed, installed, and operated during the Second World War in the United Kingdom [2]. It is considered as an appealing solution for those large offshore oil and gas fields with high revenue and limited step outs. Nevertheless, even with technological advancements, its implementation can still have several limitations. The costs related to design, installation, inspection, and maintenance can be excessively high. Besides, the maintenance of the pipelines demands an entire or sectional shut-in. These limitations make the submarine pipelines unsuitable for remote oil and gas fields with low-profit margins or in deep water. An alternative that is usually considered to make these fields feasible for production is tanker ships and liquified gas carriers. These tanker ships are very flexible to cope with situations, e.g., a suddenly increased demand, as they can quickly be deployed to the desired fields. In addition, when one tanker ship is under maintenance, a substitute tanker can be sent immediately. However, the operation of tanker ships is highly dependent on weather conditions and not suitable for severe sea states. The large wave- and wind-induced load-effects cause tremendous relative motion between the tanker ship and platform. This further increase the risk of collision and damage to hawser and flowlines.

Considering this, innovative ways to perform offshore oil production activities are being developed using autonomous marine systems, such as subsea gliders [3] and autonomous freight submarines [4]. Since these vessels are underwater, the operation is not weather dependent, i.e., it is not exposed to wind and waves, meaning it can work even in severe sea states.

Although the blueprint of utilising large submarines for freight, especially hydrocarbon, transportation was discussed back in the 1970s [5-9], it has been put on halt until recently, limited by technology. The Subsea Shuttle System concept was first unveiled in 2019. In two research disclosures, Equinor Energy AS [10, 11] proposed several types of novel subsea transportation systems to transport liquid carbon dioxide from an existing offshore/land facility where CO_2 is collected to the subsea well where it can be injected. Its purpose is to be an alternative to pipelines, umbilical, and tanker ships, especially for fields that are not economically feasible to justify full subsea installations. Later on, Xing et al. [12] studied key design considerations regarding a novel Subsea Shuttle Tanker (SST) concept. Based on this, a baseline design of SST for liquid CO_2 transportation is proposed [4]. A technical-economic feasibility study is then performed by Xing et al. [13] on the SST and found that it is more economically feasible than pipelines and tanker ships for those subsea wells within 750 km step-outs from the shore and have a capacity within 2.5 million tonnes per annual.

The SST is propelled by a single propeller during the operation and has its depth controlled by hydroplanes at the stern, but this configuration cannot hover or operate at a low forward speed. Therefore, thrusters allow control at low and zero speed to make it capable of hovering.

1.2 Hovering Control

The offloading process will be done through a flexible flowline that connects the subsea well to the SST. For that, the SST will hover at operating depth in the vicinity, and the connection/disconnection is made using a Remotely Operated Vehicle [4]. In this way, the offloading method allows the SST to offload to subsea wells located at greater depths than the nominal diving depth (70 m).

The hovering system plays an essential role in the offloading process. As illustrated in Fig. 1, the SST is subjected to different environmental disturbances during the four-hour offloading process, including hydrostatic pressure, wave (if it offloads in shallow water), buoyancy and current. The current disturbance has the most significant load effects on the SST, as these load-effects are non-uniform, time-varying and drag-dominant. When developing the manoeuvring model of the SST, the authors found that the quadratic drag hydrodynamic derivative $Y_{|v|v}$ is 80 times higher than $X_{|u|u}$ for the SST. This indicates that with the same current speed, the side-way current drag is 80 times as significant as the head-on current drag. Therefore, SST should be current-vane and constantly face current while offloading.

It is essential to have a throughout understanding of the dynamic response of the SST during offloading, as the maximum heave motion decides the maximum and minimum depth. The maximum depth drives to the extreme hydrostatic pressure acting on the SST during the operation, which dominates the collapse depth and SST pressure hull design. The minimum depth determines the upper bounds of the safety depth of the

SST. In addition, the surge motion of the SST affects the required length of the hose to reduce the risk of stretching or snap loadings on the connection joint.

The hovering system can directly impact the efficiency of the SST. Since it can consume more energy than necessary if not designed wisely to deal with the operating environmental condition. Also, the safety of operation, collision avoidance, and station-keeping in currents have to be considered during the controller design. Therefore, Linear Quadratic Regulator (LQR) is used to study the SST hovering control problem. LQR is an optimal full-state feedback controller that finds the feedback gains of a given system by achieving a specific optimality criterion [14]. It optimizes a cost function $\boldsymbol{L}(\boldsymbol{x}(t), \boldsymbol{u}(t))$ as expressed in (16), which is a sum of weighted performance and actuator effort. Its application on marine crafts includes heading autopilot, rudder-roll damping system and dynamic positioning system [15]. As for Autonomous Underwater Vehicles (AUV), Mendes et al. [16] evaluated the waypoint tracking problem of an AUV by using a Proportional-Integral-Derivative (PID) controller and an LQR. The study found that the responsiveness of an LQR is more excellent than PID. Tiwari and Sharma [17] analysed the hovering control of an AUV with an LQR. The study indicated that it enables the AUV to hover with the minimum number of undesired oscillations and low power consumption at the desired depth.

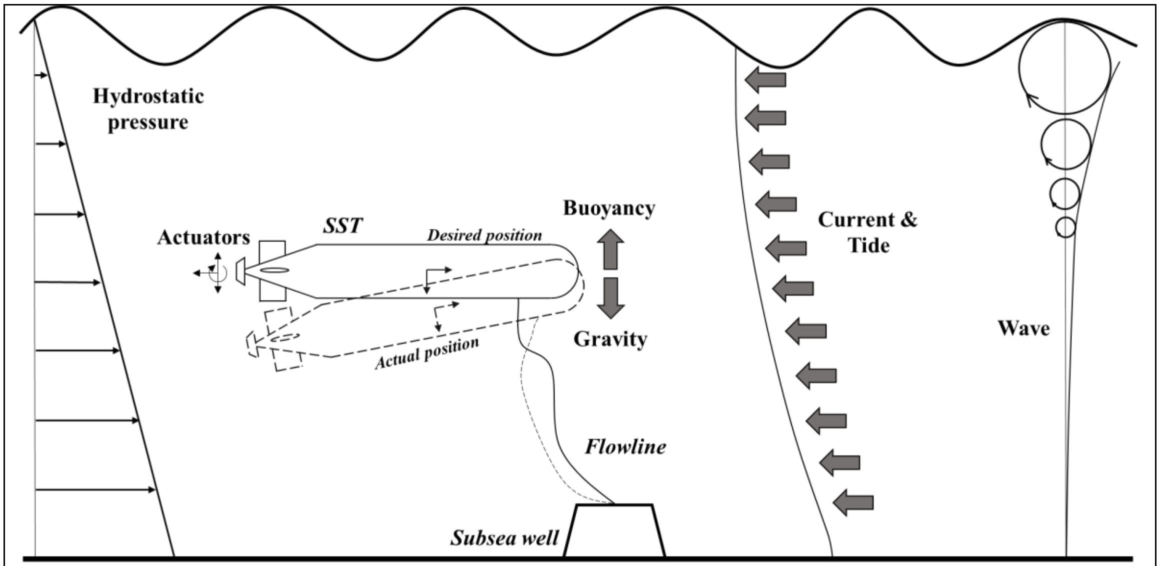

Fig. 1 Environmental loads on the SST

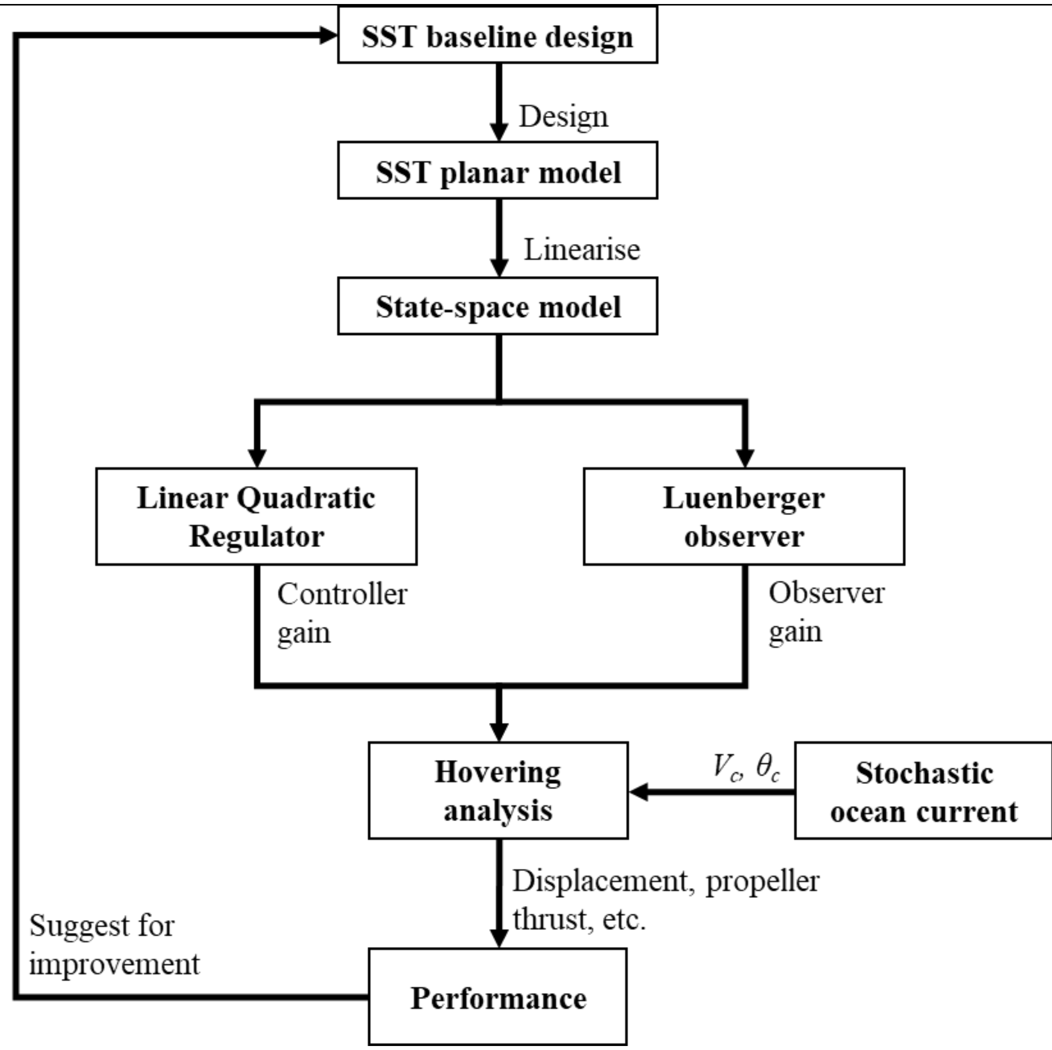

Fig. 2 Hovering analysis flowchart.

This paper targets to develop a comprehensive manoeuvring model and an LQR control for hovering the SST in stochastic current. A flowchart of the model developed in this work is presented in Fig. 2. First, an SST manoeuvring planar model is developed based on the existing baseline design [4]. The SST utilizes its two vertical tunnel thrusters and main propeller to handle the external loads. Second, a simplified state-space model is linearised from the planar model. This linear state-space model is later used to determine the LQR controller gain and Luenberger observer gain. After that, the LQR is used to obtain the hovering control input $\boldsymbol{u}(t)$. The incoming current follows a first-order Gauss-Markov process in both current velocity and inflow angle. The SST states are measured by a Luenberger observer. The model developed in this paper helps to contribute knowledge on the manoeuvring and hovering analysis for the future extra-large AUVs which are under development aiming to reduce the carbon footprint and better utilise the vast ocean space. The model presented in this paper can be used to answer some of the most critical questions and helps to improve the conceptual design.

2 SUBSEA SHUTTLE TANKER PLANAR MODEL

2.1 SST Design Parameters

The UiS baseline SST has a length of 164 m and a beam of 17 m. It travels at 70 m constant water depth at a 6 knots slow speed [4]. The most critical design parameters of the SST are displaced in Table 1.

Table 1 Subsea shuttle tanker configuration

Parameter	**Value**	**Unit**
Length	164	m
Beam	17	m
Total mass m	3.36×10^7	kg
Pitch moment of inertia I_{yy}	3.63×10^9	kg·m^2
Centre of buoyancy $[x_b, y_b, z_b]$	[0, 0, -0.41]	m
Skeg position x_s	67	m
Skeg area A_S	40	m^2
Skeg lift rate coefficient	6.1	
Forward tunnel thruster position x_{tf}	60	m
Aft tunnel thruster position x_{ta}	-60	m
Tunnel thruster diameter d_t	2	m
Tunnel thruster thrust coefficient K_{Tt}	0.4	-
Main propeller diameter d_p	7	m
Main propeller thrust coefficient K_{Tp}	0.19	-
Carbon dioxide capacity	1.7×10^6	kg

2.2 Manoeuvring Model Formulation

2.2.1 Coordinate system

The vehicle body-fixed coordinate system locates at the vehicle's centre of gravity. The motion of the body-fixed frame of reference is relative to an earth-fixed global reference frame (North, East, and Down). The centre of buoyancy locates right above the centre of gravity at the SST's geometric centre. The coordinate system is presented in Fig. 3.

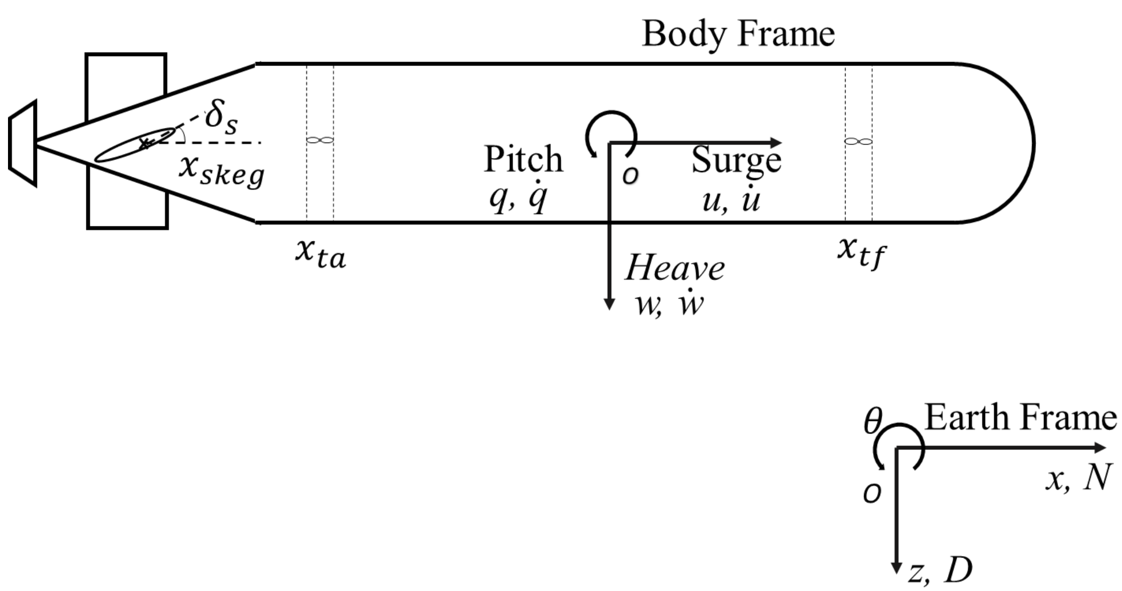

Fig. 3 SST coordinate system setup

In the figure, x and z are translational motion in the global coordinate system; θ is the pitch rotational motion; u, w, and q are surge velocity, heave velocity, and pitch velocity, respectively; $\dot{u}$, $\dot{w}$, and $\dot{q}$ are the corresponding accelerations.

2.2.2 Plant model

The SST equations of motion, including surge, heave and pitch motions, can be expressed as kinematic equations (1) and dynamic equations (2) in the vectorial form:

$\dot{\boldsymbol{\eta}} = \boldsymbol{J}_{\boldsymbol{\Theta}}(\boldsymbol{\eta})\boldsymbol{\nu}$	(1)
$\boldsymbol{M}\dot{\boldsymbol{\nu}} + \boldsymbol{C}(\boldsymbol{\nu})\boldsymbol{\nu} + \boldsymbol{D}(\boldsymbol{\nu})\boldsymbol{\nu} + \boldsymbol{g}(\boldsymbol{\eta}) = \boldsymbol{\tau}$	(2)

where $\boldsymbol{\eta}$ is SST NED position and Euler angles; $\boldsymbol{\nu}$ is the velocity components in the body-fixed system; $\boldsymbol{J}_{\boldsymbol{\Theta}}(\boldsymbol{\eta})$ is the Euler transformation matrix; $\boldsymbol{M}$ is the system mass matrix, which includes the mass and added mass of the SST; $\boldsymbol{C}(\boldsymbol{\nu})$ is the Coriolis-centripetal matrix; $\boldsymbol{D}(\boldsymbol{\nu})$ is the hydrodynamic damping matrix; $\boldsymbol{g}(\boldsymbol{\eta})$ is a force vector considering hydrostatic forces, $\boldsymbol{\tau}$ is the control force vector.

The kinematic component can be expanded with Euler angle representation and be presented as:

$\underbrace{\begin{bmatrix} \dot{N} \\ \dot{D} \\ \dot{\theta} \end{bmatrix}}_{\dot{\boldsymbol{\eta}}} = \underbrace{\begin{bmatrix} \cos\theta & \sin\theta & 0 \\ -\sin\theta & \cos\theta & 0 \\ 0 & 0 & 1 \end{bmatrix}}_{\boldsymbol{J}_{\boldsymbol{\Theta}}(\boldsymbol{\eta})} \underbrace{\begin{bmatrix} u \\ w \\ q \end{bmatrix}}_{\boldsymbol{\nu}}$	(3)

where $\dot{\boldsymbol{\eta}}$ is the velocity vector in the global NED frame; θ is SST pitch angle; u, w, and q are surge, heave, and pitch velocity in the body frame, respectively. The motions and velocities are illustrated in Fig. 1.

$$\boldsymbol{M} = \begin{bmatrix} m - X_{\dot{u}} & 0 & mz_g \\ 0 & m - Z_{\dot{w}} & -Z_{\dot{q}} \\ mz_g & M_{\dot{w}} & I_{yy} - M_{\dot{q}} \end{bmatrix} \tag{4}$$

$$\boldsymbol{C}(\boldsymbol{\nu}) = \begin{bmatrix} 0 & 0 & 0 \\ 0 & m - Z_{\dot{w}} & -(m - X_{\dot{u}})u \\ 0 & (Z_{\dot{w}} - X_{\dot{u}}) & 0 \end{bmatrix} \tag{5}$$

$$\boldsymbol{D}(\boldsymbol{\nu}) = \begin{bmatrix} X_{|u|u}|u| & X_{wq}q & X_{qq}q \\ Z_{uq}q & Z_{|w|w} + Z_{uw}u & Z_{q|q|} \\ M_{uw}w & M_{|w|w} & M_{uq}u + M_{|q|q} \end{bmatrix} \tag{6}$$

where $X_{\dot{u}}$, $Z_{\dot{w}}$, $Z_{\dot{q}}$, $M_{\dot{w}}$, and $M_{\dot{q}}$ are added mass hydrodynamic derivatives; $X_{|u|u}$, $Z_{|w|w}$, $Z_{|q|q}$, $M_{|w|w}$, and $M_{|q|q}$ are hydrodynamic drag derivatives; X_{wq}, X_{qq}, Z_{uw}, Z_{uq}, and M_{uq} are added mass hydrodynamic derivative cross-terms. Z_{uw} and M_{uw} are the body lift and Munk moment.

Table 2 Hydrodynamic derivatives

Parameter	Value	Unit	Parameter	Value	Unit
$X_{\dot{u}}$	-5.14×10^{5}	kg	$Z_{\|q\|q}$	4.79×10^{9}	kg·m
$Z_{\dot{w}}$	-3.29×10^{7}	kg	$M_{\|q\|q}$	-4.34×10^{12}	kg·m^2
$M_{\dot{w}}$	-4.40×10^{8}	kg·m	X_{wq}	-3.28×10^{7}	kg
$Z_{\dot{q}}$	-4.40×10^{8}	kg·m	X_{qq}	-4.40×10^{8}	kg·m
$M_{\dot{q}}$	-6.39×10^{10}	kg·m^2	Z_{uq}	5.14×10^{5}	kg
$X_{\|u\|u}$	-1.64×10^{4}	kg/m	M_{uq}	-4.40×10^{8}	kg·m
$Z_{\|w\|w}$	-1.42×10^{6}	kg/m	Z_{uw}	-2.42×10^{5}	kg/m
$M_{\|w\|w}$	1.67×10^{7}	kg	M_{uw}	-3.99×10^{7}	kg

2.2.3 Control plane

The SST equips two bow control planes and two aft control planes locating at the port and starboard sides to control its depth. The lift force generated by a control plane is expressed as (7):

$$\tau_s = 0.5\rho C_L S_{skeg}(\delta_s - \theta)u^2 \tag{7}$$

where $\rho = 1025\ kg \cdot m^3$ is seawater density, C_L is the lift rate coefficient of skegs, $S_{skeg} = 40\ m^2$ is the skeg area, δ_s is the skeg angle. In the design, the SST uses Bower's airfoil profile [18]. δ_s is fixed to 0 radius and $C_L = 6.1\ rad^{-1}$ is used.

2.2.4 Thruster

As shown in Fig. 3, the SST uses two identical tunnel thrusters: one forward thruster and one aft thruster. Their locations are listed in Table 1. The thruster thrust τ_t is calculated as (8). This equation is used to calculate forward thruster thrust τ_{tf} and aft thruster thrust τ_{ta}.

$$\tau_t = K_{Tt} \cdot \rho \cdot n_t^2 \cdot d_t^4 \tag{8}$$

where $K_{Tt} = 0.4$ is the thrust coefficient, n_t is the thruster rotational speed, and d_t is the thruster diameter. The diameter of the SST tunnel thruster is estimated to be 2 m, close to current Kongsberg marine tunnel thrusters [19]. A single designed propeller can provide a maximum 164 kN thrust at 300 RPM, and this is equivalent to the side-way drags at 1-knot heave speed. Simulation results in Section 4 proved that this design could provide enough thrust for the designed current speed during hovering.

3.2.5 Main propeller

The initial design of the SST propeller is performed in the baseline design [4]. A 3-bladed Wageningen B-series propeller is used on the SST. The propeller diameter d_p is 7 m and its thrust coefficient K_{Tp} is 0.19. The propeller thrust force can therefore be obtained from (9):

$\tau_p = K_{Tp} \cdot \rho \cdot n_p^2 \cdot d_p^4$	(9)

where n_p is propeller rotational speed.

2.3 Stochastic Ocean Current

The stochastic ocean current model used in this paper is introduced by Fossen [15] and Sørensen [20]. Both current velocity and current direction are described as a first-order Gauss-Markov process. The current profile is presented in (10) and (11):

$\dot{V}_c + \mu_1 V_c = \omega_1$	(10)
$\dot{\theta}_c + \mu_2 \theta_c = \omega_2$	(11)

where V_c is current speed and θ_c is the inflow angle, μ_1 and μ_2 are constants related to the time constant of the Gauss-Markov process. ω_1 and ω_2 are Gaussian white noise.

According to Fossen [15], the constants μ_1 and μ_2 should be non-negative. They affect the rise time before a steady state is reached. In this study, a small value 1 is used for both constants to reduce the rise time and generate a steady-state current. Mean current speed at 0.5 m/s, 1 m/s, and 1.5 m/s are studied.

The designed current speed is 1 m/s for the baseline SST. This value is close to the 0.96 m/s highest seasonal current velocities measured by Bruserud and Haver in the northern North Sea [21]. Also, the Norwegian Petroleum Directorate [22] indicates that the Norwegian Coastal Current, which can be traced from north Scotland and the eastern North Sea at depths up to 100 m, can easily exceed 1 m/s speed.

It should be noticed that the current speed is expressed in the global NED frame, and it is then transformed into the SST body-fixed frame and added to SST velocity to calculate the hydrodynamic forces.

2.4 Simulink Implementation

Following the above-mentioned mathematical formulation, a Simulink model is built and presented in Fig. 4. The model is divided into three blocks:

- Plant model: The plant model represents the equations of motion of the SST body. It considers the hydrodynamic properties of the SST, including the added mass, damping, and body lift forces.
- Actuators: This is the block consisting of all contributions from the actuators, including propeller, skeg (hydroplane), ballast tanks, and thrusters. In this study, the ballast tank is modelled as a constant mass ensuring the neutral buoyant of the SST. The modelling of other components is described in **Section 2.2**.
- Current: The current velocity is generated in this block following the methodology presented in **Section 2.3**. It is added together with SST velocity to obtain the relative velocity between SST and flow.

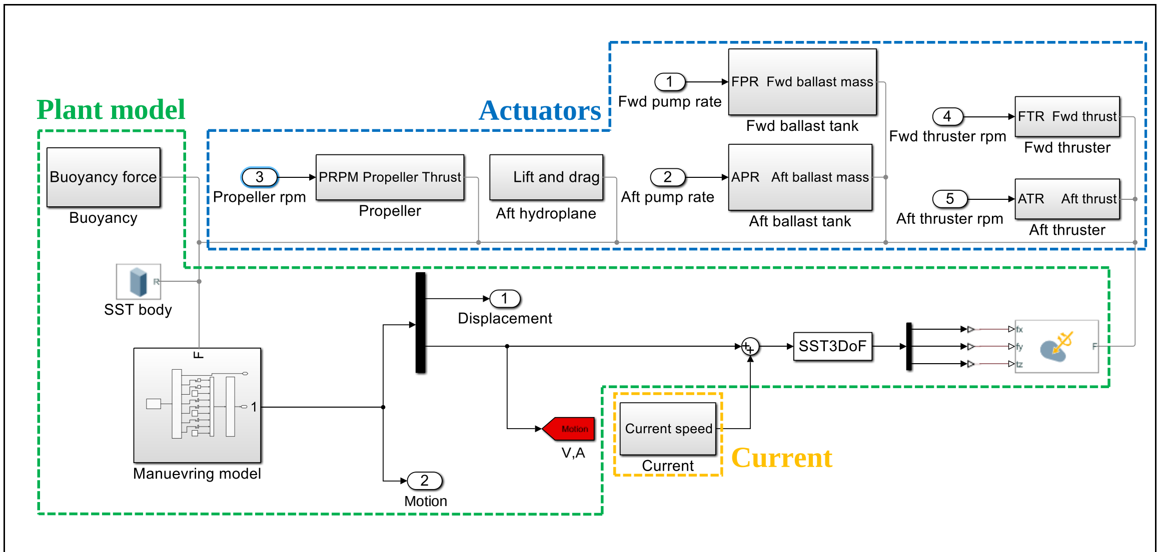

Fig. 4 Simulink dynamic model

3 CONTROL SYSTEM DESIGN

This section introduces the design of the SST hovering control system. A block diagram demonstrating the control loop of the SST hovering problem is presented in Fig. 5. The layout of this control diagram is similar to a full state feedback control system with observation. As shown in the diagram, the actuator control input $\boldsymbol{u}$ is first calculated from state feedback and trajectory reference. Then it is transferred into the SST manoeuvring together with current disturbances to obtain the output $\boldsymbol{y}$. An observer is used to measure the SST states. It takes in system control input $\boldsymbol{u}$ and system output $\boldsymbol{y}$. It outputs the estimated state $\hat{\boldsymbol{x}}$. After this, estimated states multiply the controller gain to obtain the feedback, which will be finally used to obtain $\boldsymbol{u}$.

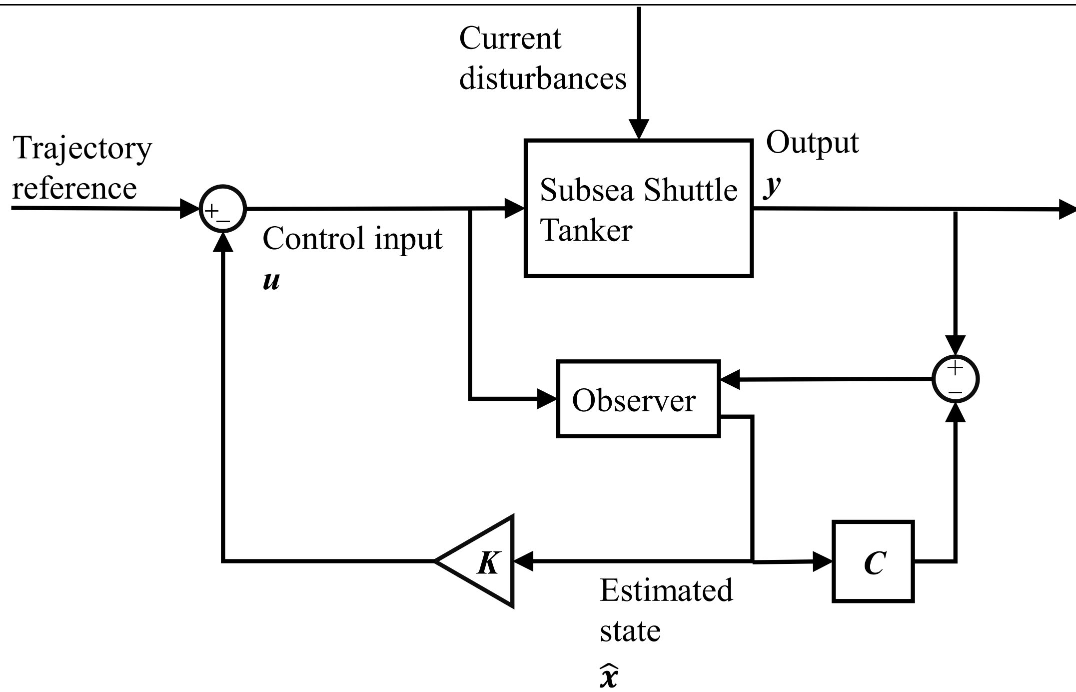

Fig. 5 SST control diagram

3.1 Linear State-space Model

3.1.1 Linear state-space function

A linear state-space model is required to design an LQR controller. The linear input-output state-space representation of SST is described as a time-invariant system by a pair of equations (12):

$$\dot{\boldsymbol{x}} = \boldsymbol{A}\boldsymbol{x} + \boldsymbol{B}\boldsymbol{u}$$
$$\boldsymbol{y} = \boldsymbol{C}\boldsymbol{x} \tag{12}$$

where $\boldsymbol{x}$ is the state vector, $\boldsymbol{y}$ is the output vector, $\boldsymbol{u}$ is the control input vector (also shown in Fig. 5). $\boldsymbol{A}$ is state matrix, $\boldsymbol{B}$ is input matrix, and $\boldsymbol{C}$ is output matrix.

3.1.2 Model linearisation

However, as previously presented, the SST manoeuvring model is highly nonlinear, coupled, and time-dependent. However, linearised time-invariant $\boldsymbol{A}$ and $\boldsymbol{B}$ are required to determine the controller gain. The linear state-space function is obtained through model linearisation to cope with this. MATLAB model lineariser is used in this process. The input of the linearised model is set to be $\boldsymbol{u} = [n_{tf}; n_p; n_{ta}]$, i.e., the revolution speed of front tunnel thruster, main propeller, and aft tunnel thruster. The outputs of the model are the variants to be controlled. It is set as $\boldsymbol{y} = [N; D; \theta]$, i.e., longitudinal motion, vertical motion, and pitch motion. Consequently, the state vector $\boldsymbol{x} = [N; D; \theta; \dot{N}; \dot{D}; \dot{\theta}]$ is obtained. The adopted linearisation is performed at the operating point with a current velocity of 1 m/s design current speed and a 1 ° small-angle heading. A sensitivity study is later performed. As a result, it can be seen from (12) that $\boldsymbol{A}$ is a 6 by 6 matrix, $\boldsymbol{B}$ is a 6 by 3 matrix, and $\boldsymbol{C}$ is a 3 by 6 matrix as listed in (13) to (15):

$\boldsymbol{A} = \begin{bmatrix} 0 & 0 & 0 & 1 & 0 & 0 \\ 0 & 0 & 0 & 0 & 1 & 0 \\ 0 & 0 & 0 & 0 & 0 & 1 \\ 0 & 0 & 2.65 \times 10^{-5} & -1.00 \times 10^{-3} & -1.21 \times 10^{-4} & -1.45 \times 10^{-2} \\ 0 & 0 & 2.87 \times 10^{-6} & -1.32 \times 10^{-4} & -8.91 \times 10^{-3} & 5.18 \times 10^{-2} \\ 0 & 0 & -2.37 \times 10^{-2} & 6.21 \times 10^{-5} & 3.87 \times 10^{-3} & -5.96 \times 10^{-2} \end{bmatrix}$	(13)
$\boldsymbol{B} = \begin{bmatrix} 0 & 0 & 0 \\ 0 & 0 & 0 \\ 0 & 0 & 0 \\ 2.54 \times 10^{-10} & -8.80 \times 10^{-5} & 4.24 \times 10^{-10} \\ 3.84 \times 10^{-6} & -5.25 \times 10^{-9} & 6.40 \times 10^{-6} \\ 7.13 \times 10^{-7} & 0 & -1.19 \times 10^{-6} \end{bmatrix}$	(14)
$\boldsymbol{C} = \begin{bmatrix} 1 & 0 & 0 & 0 & 0 & 0 \\ 0 & 1 & 0 & 0 & 0 & 0 \\ 0 & 0 & 1 & 0 & 0 & 0 \end{bmatrix}$	(15)

3.2 Linear Quadratic Regulator

LQR is an optimal control method. Therefore, the controller finds the gain matrix by solving an optimisation problem. LQR finds the control law for linear time-invariant systems (expressed as (12)) by solving quadratic cost functions [15]. It regulates the outputs $\boldsymbol{y}$ of the system to a constant value. The minimised quadratic cost function is expressed as:

$$\boldsymbol{L}(\boldsymbol{x},\boldsymbol{u}) = \int_0^\infty (\boldsymbol{x}^T\boldsymbol{Q}\boldsymbol{x} + \boldsymbol{u}^T\boldsymbol{R}\boldsymbol{u})dt \tag{16}$$

where $\boldsymbol{Q} = \boldsymbol{Q}^T \geq 0$ is the state weighting matrix and $\boldsymbol{R} = \boldsymbol{R}^T > 0$ is the actuator energy weighting matrix, which determines the importance of state error and energy expenditure, respectively. The targeted states can be penalized by adjusting the corresponding diagonal elements in $\boldsymbol{Q}$. Similarly, targeted actuator efforts can be controlled by adjusting corresponding elements in $\boldsymbol{R}$.

The equivalent control law for an LQR is:

$$\boldsymbol{u} = -\boldsymbol{K}\boldsymbol{x} \tag{17}$$

where $\boldsymbol{K}$ is a 3 by 6 gain matrix.

In order to design an LQR, the SST planar model must be controllable. This means the linear state matrix $\boldsymbol{A}$ and linear input matrix $\boldsymbol{B}$ both have to satisfy the controllability condition, . Tt the controllability matrix $\boldsymbol{Con}$ must have full row rank and therefore have a right inverse [23]. The controllability matrix is obtained as (18):

$$\boldsymbol{Con} = [\boldsymbol{B}|\boldsymbol{AB}|\cdots|\boldsymbol{A}^{n-1}\boldsymbol{B}\ ] \tag{18}$$

The linearised model is controllable as it has a controllability matrix with rank 6.

3.3 Luenberger Observer

A linear regulator controller development leads to a state variable feedback law. This means an optimal control method uses the observation of all state variable components to calculate the control input [24]. One way of performing such measurement is applying a Luenberger observer [23] to represent sensors and providing state measurement to the SST. As shown in Fig. 5, the Luenberger observer is a simple fixed-gain observer. It reconstructs the estimated state $\hat{\boldsymbol{x}}$ from control input $\boldsymbol{u}$ and system output $\boldsymbol{y}$. The estimated state vector $\hat{\boldsymbol{x}}$, instead of actual state vector $\boldsymbol{x}$, will then be used as the state feedback to obtain the control input for the next time step. The continuous time Luenberger observer can be described by the following differential equation:

$$\dot{\hat{\boldsymbol{x}}} = \boldsymbol{A}\hat{\boldsymbol{x}} + \boldsymbol{B}\boldsymbol{u} + \boldsymbol{K_L}(\boldsymbol{y} - \hat{\boldsymbol{y}}) \quad (19)$$

where $\boldsymbol{K_L}$ is the observer gain, $\hat{\boldsymbol{y}}$ is the estimated output vector. The observer gain is obtained by placing the close loop poles on the negative side of the real axis.

Before implementing the observer, the observability of the linearised model is checked. The observability infers how well one can estimate the real-time state $\boldsymbol{x}$ from the actuator input $\boldsymbol{u}$ and system output $\boldsymbol{y}$. Similar to the controllability matrix, the observability matrix $\boldsymbol{Obs}$ can be expressed as a matrix consists of the transpose of the linear state matrix $\boldsymbol{A}$ and linear output matrix $\boldsymbol{C}$.

$$\boldsymbol{Obs} = [\boldsymbol{C}^\top | \boldsymbol{A}^\top \boldsymbol{C}^\top | \cdots | (\boldsymbol{A}^\top)^{n-1} \boldsymbol{C}^\top] \quad (20)$$

The linearised SST state-space model is observable, i.e., all states can be obtained through the output sensor, as the observability matrix (20) has full column rank 6.

4 RESULTS

4.1 Linearisation Point Steady State Sensitivity Analysis

The SST linear state-space model is obtained from linearising the manoeuvring model at a steady state with constant current speed and fixed inflow angle. In this process, the SST's stationary is maintained by two tunnel thrusters and the propeller, which are controlled by three independent PID controllers. The measured input points are the front thruster revolution, aft thruster revolution, and propeller revolution. Surge, heave, and pitch motion in the global frame are the measured outputs. The selected current velocity and inflow angle affect both the state and input matrix in this process. Steady-state sensitivity analysis is therefore performed to better understand such effects.

The SST manoeuvring model is linearised at four different steady points. For each controller gain, the $\boldsymbol{Q}$ matrix is set to an identity matrix. The diagonal values in $\boldsymbol{R}$ matrix is set to $[1 \times 10^{-2}; 1 \times 10^{-4}; 1 \times 10^{-4}]$ for main propeller, front tunnel thruster, and aft tunnel thruster, respectively. Same values are used in weighting matrixes for different state-space functions to ensure that the results are comparable. All linear state-space models are linearised at 1 m/s constant current speed. Moreover, four different current inflow angles are selected. These angles are 1 °, 5 °, 10 °, and 15 °.

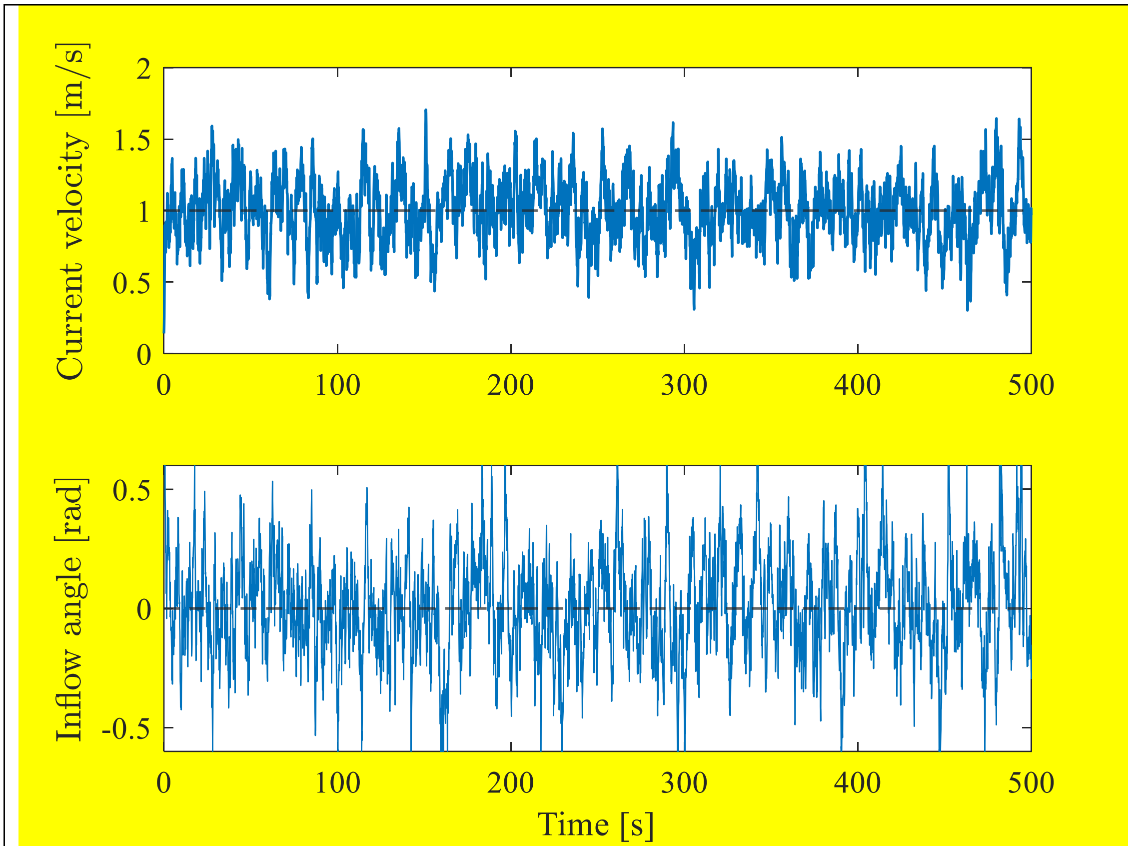

Fig. 6 Inflow current realisation.

380

381 Fig. 6 exemplifies a 500-second realisation of the incoming current speed and inflow angle. In the linearisation point study, the mean current velocity is 1 m/s, and the mean inflow angle is 0 rad. Fig. 7 presents the hovering performances of the SST with the controller gain calculated from the linear state-space model obtained from the above-mentioned linearisation points. Moreover, the same current profile is used. From the figure, it can be noticed that although the performances of the controller gains are different, all systems are still stable, i.e., the SST maintains its position while hovering. This indicates that the stability of this closed-loop system is not sensitive to the selected linearisation points. However, the linearisation point affects the heave and surge

motions. The result of surge motion is presented in Fig. 7 (up). From the figure, a transient time of approximately 200 s is observed. The SST is pushed backwards by the current. This steady offset is the same for all four cases and is approximately 1.2 m. As for the performance of different controller gains', the amplitude of fluctuation decreases with the linearisation inflow angle, the minimum fluctuation is observed for $\theta_c = 1°$. Linearised at 15 ° returns with a significantly worse result in surge motion.

When it comes to the surge motion (presented in Fig. 7 down), the difference in maximum offset is moderate. However, the maximum response can still be observed in the 15 ° case. In the listed cases, linearising the model at a smaller inflow angle (1 °) can lead to a controller gain with better performance in the heave direction.

Due to the significant hydrostatic restoring force, pitch motion is negligible in the SST hovering problem. Nevertheless, the negative maxima can be found at 500 s on the 15 ° case.

It should also be noted that the SST linear model cannot be obtained when the linearisation point is 0 °. This is because, with a 0 ° angle of attack, the contribution from tunnel thrusters is not captured. Therefore, the linearised state-space model obtained from linearisation at 1 m/s steady current speed, 1 ° angle of attack is used in this study.

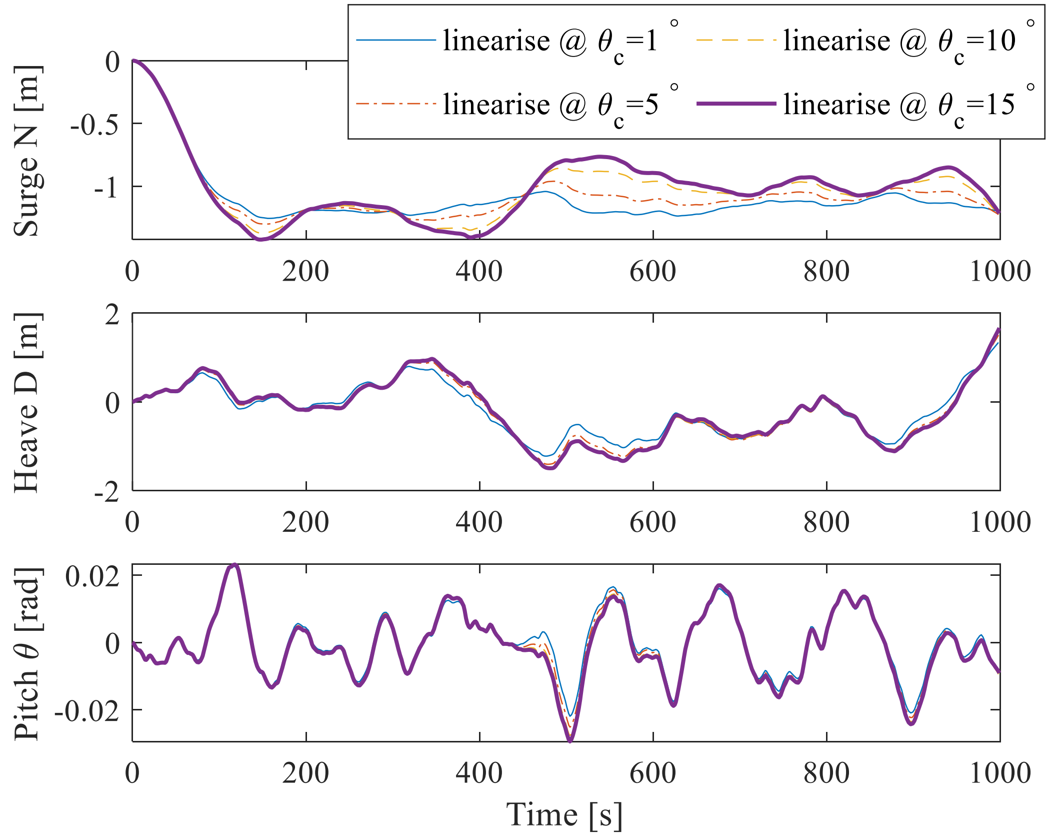

Fig. 7 SST hovering control performance for state-space models obtained at different linearisation points.

407

408

4.2 Observer Pole-placement Analysis

The observability matrix $\boldsymbol{Obs}$ of the SST linear state-space model is non-singular, i.e., it has a total column rank 6. Therefore, the poles of the error dynamics can be placed in the negative half-plane to ensure stability [15]. However, as the desired closed-loop pole positions for the SST observer are not explicit, a sensitivity analysis is performed to find the observer pole position with less error. In this section, four sets of pole positions are selected as listed in Table 3. All closed-loop poles are placed on the left half-plane but at different distances from the origin.

Table 3 Observer pole position

	N	D	θ	$\dot{N}$	$\dot{D}$	$\dot{\theta}$
Pole position 1 (P1)	-0.5	-0.5	-0.5	-0.2	-0.2	-0.2
Pole position 2 (P2)	-2	-2	-2	-1	-1	-1
Pole position 3 (P3)	-4	-4	-4	-2	-2	-2
Pole position 4 (P4)	-8	-8	-8	-4	-4	-4

The results of the four cases, including measurement and actual motion, are presented in Fig. 8. In this simulation, the mean current speed is set to 1 m/s. State-space model linearised at 1 ° inflow angle is selected as it can provide the best performance. Still, the $\boldsymbol{Q}$ matrix is set to identity matrix and the diagonal values in $\boldsymbol{R}$ matrix is set to $[1 \times 10^{-2}; 1 \times 10^{-4}; 1 \times 10^{-4}]$ to calculate the controller gain. The Luenberger observer can provide measurements for all cases according to simulation results. However, smaller errors are found for the observer whose poles are close to 0 (Observer P1). On the contrary, the error in P2, P3, and P4 are negligible. In addition, a smaller measurement error can be found in heave than in surge or pitch, even when the same pole position is used, as shown in Table 3.

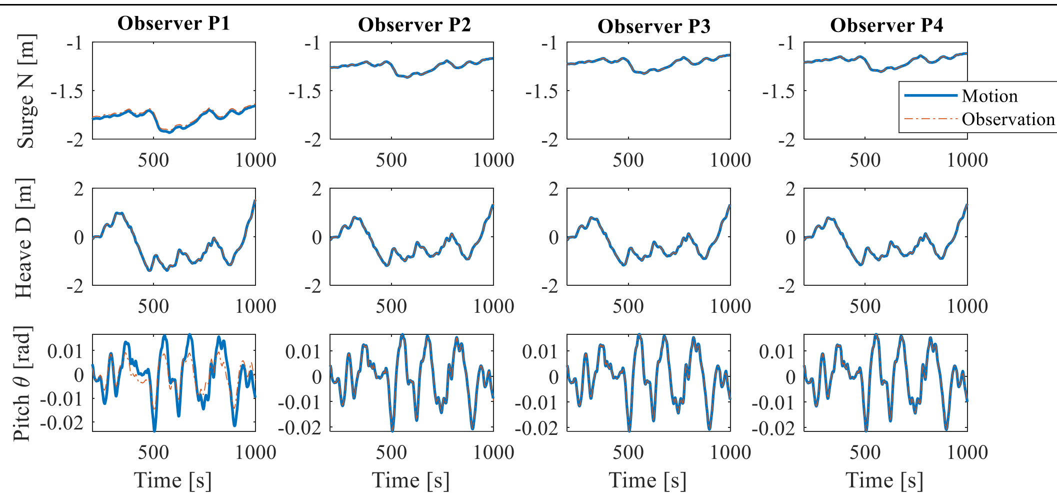

Fig. 8 Effects of observer gain on SST motions.

The observer's closed-loop pole positions also affect the performance of the controller. That is, less offset is induced when the poles are placed further left. In Fig. 8, P3 and P4 deliver slightly better performance than P2 in the surge. The steady offsets of P2, P3, and P4 are much smaller than P1. The displacements in heave for all observer gains are at the same order. Still, the results of P2, P3, and P4 are similar and advantageous over P1. As for pitch motion, the difference between the four cases can be neglected, as the trim angle of the SST is balanced by hydrostatic restoring force rather than tunnel thrusters. It also can be noticed from Fig. 8 that the difference in performance between P3 and P4 is not apparent, which suggests that putting pole positions further left does not significantly improve the performance anymore. Therefore, pole positions in P3 are used to obtain the observer gain.

4.3 SST Trajectory

The designed current speed of the SST is 1 m/s [4]. This is the highest seasonal average current speed observed in the North Atlantic and Norwegian Coastal currents [22, 25, 26]. Therefore, this work studies the SST's trajectory envelope under three current conditions, i.e., 0.5 m/s, 1m/s, and 1.5 m/s mean current speeds. They represent the low current, designed current, and extreme current conditions, respectively. A four-hour simulation is performed for each current speed corresponding to the time span of a loading or offloading operation.

The performance weight matrix $\boldsymbol{Q}$ is set to be identity and the diagonal values in $\boldsymbol{R}$ matrix is set to $[1 \times 10^{-2}; 1 \times 10^{-4}; 1 \times 10^{-4}]$. As a result, the time series in the surge, heave, and pitch motions of the SST under 0.5 m/s, 1 m/s, and 1.5 m/s current speeds are presented in Fig. 9. From the figure, it can be noticed that the closed-loop system is stable. The amplitude for all motions increases with the mean inflow velocity. The largest surge displacement for 0.5 m/s, 1.0 m/s, and 1.5 m/s cases are -0.79 m, -1.38 m, and -2.04 m respectively. As for heave, the maximum observed value for V_c=0.5 m/s case is 1.18 m. It increases to 1.70 m for V_c=1.0 m/s and 2.63 m for V_c=1.0 m/s. The pitch motions are not small for all three cases. The observed maxima are 0.016 rad, 0.032 rad, and 0.044 rad for 0.5 m/s, 1.0 m/s, and 1.5 m/s current speeds, respectively.

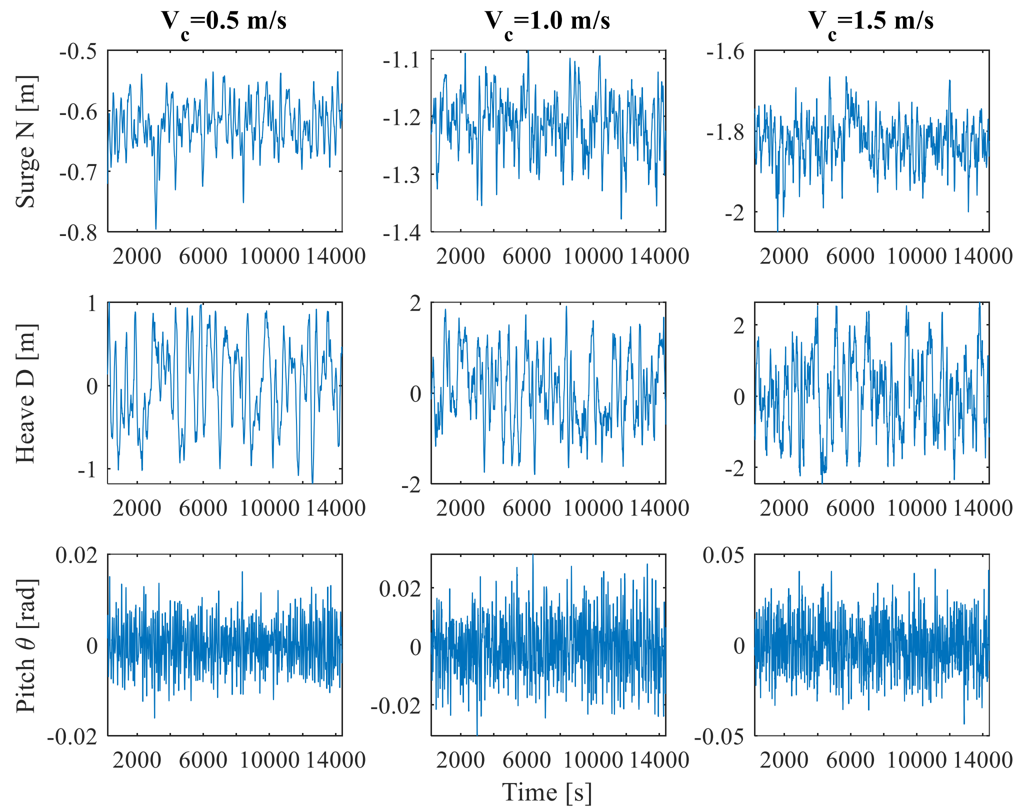

Fig. 9 Time series of SST motion under various current speeds.

Fig. 10 demonstrates the required propeller and thruster thrusts. Because the SST is a slender body with a slenderness ratio of 9.65, its side-way drag is significantly higher than the heading drags during offloading. Therefore, the required thrusts for the tunnel thrusters are also higher than the required thrust for the main propeller. Fig. 11 summarises the result of the propeller thrust time series. When facing 0.5 m/s current speed, the mean thrust is 4.7 kN, while the maximum required thrust is 9.1 kN. When the mean inflow speed is 1 m/s, the mean thrust is 17.9 kN while the maxima is 37.9 kN. For the 1.5 m/s extreme current case, the average thrust is 40.6 kN, while the maximum required thrust is 68.2 kN.

As for tunnel thrusters, the required thrusts for the front and aft thrusters are highly correlated. However, the aft controller provides more thrust than the front thruster. The highest thrusts in four simulations are 35.6 kN, 126.3 kN, and 320.1 kN for 0.5 m/s, 1.0 m/s, and 1.5 m/s current speeds, respectively. It grows proportional to the square of inflow velocity. As a result, the existing ship use tunnel thrusters [19] can fulfil the need of the SST under designed current speed.

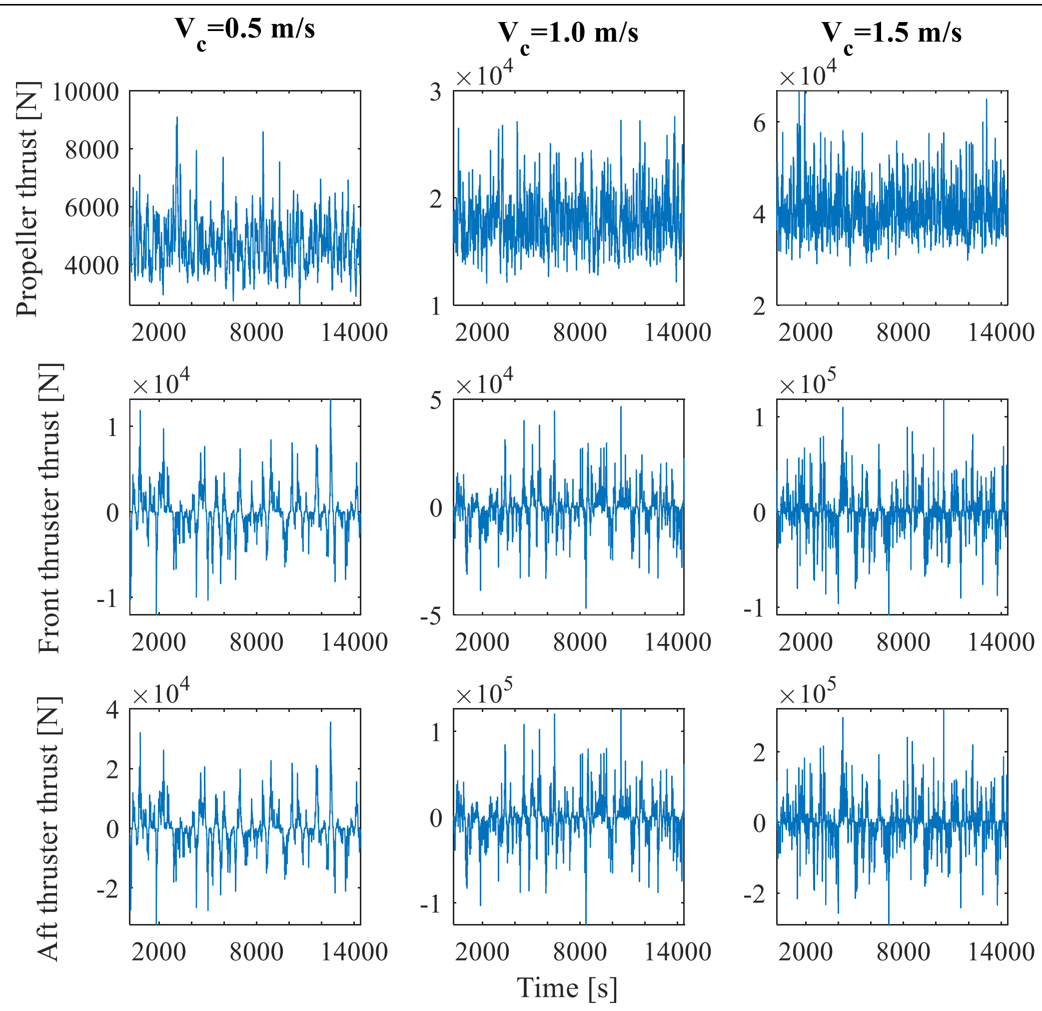

Fig. 10 SST propeller and thruster thrust.

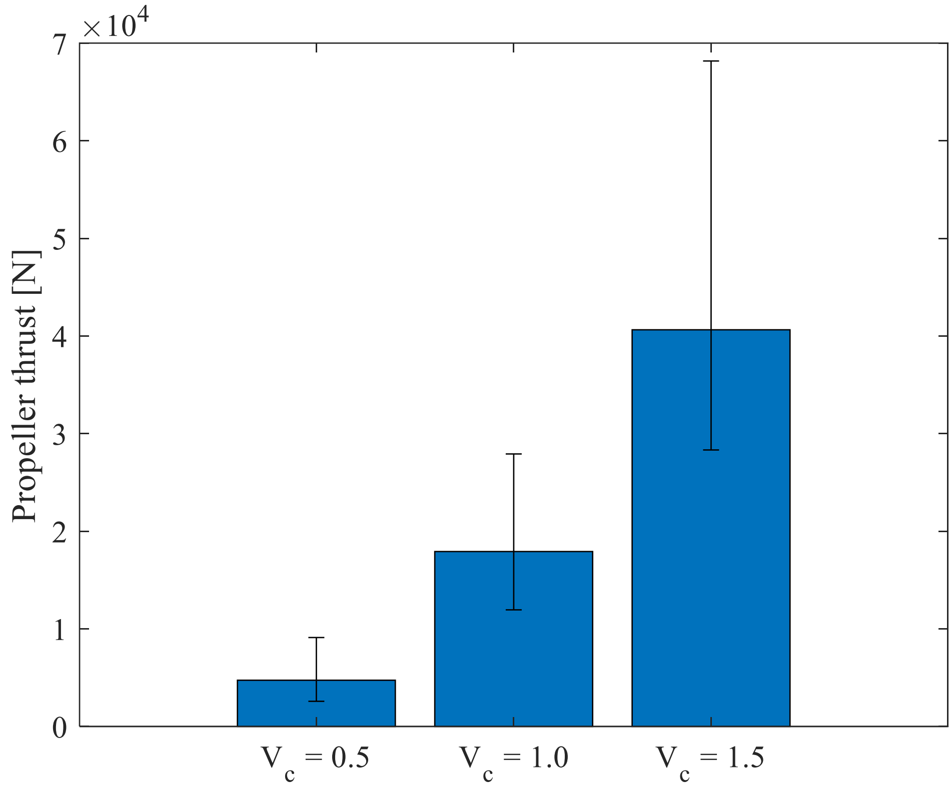

Fig. 11 Propeller mean thrust during the four-hour realisation.

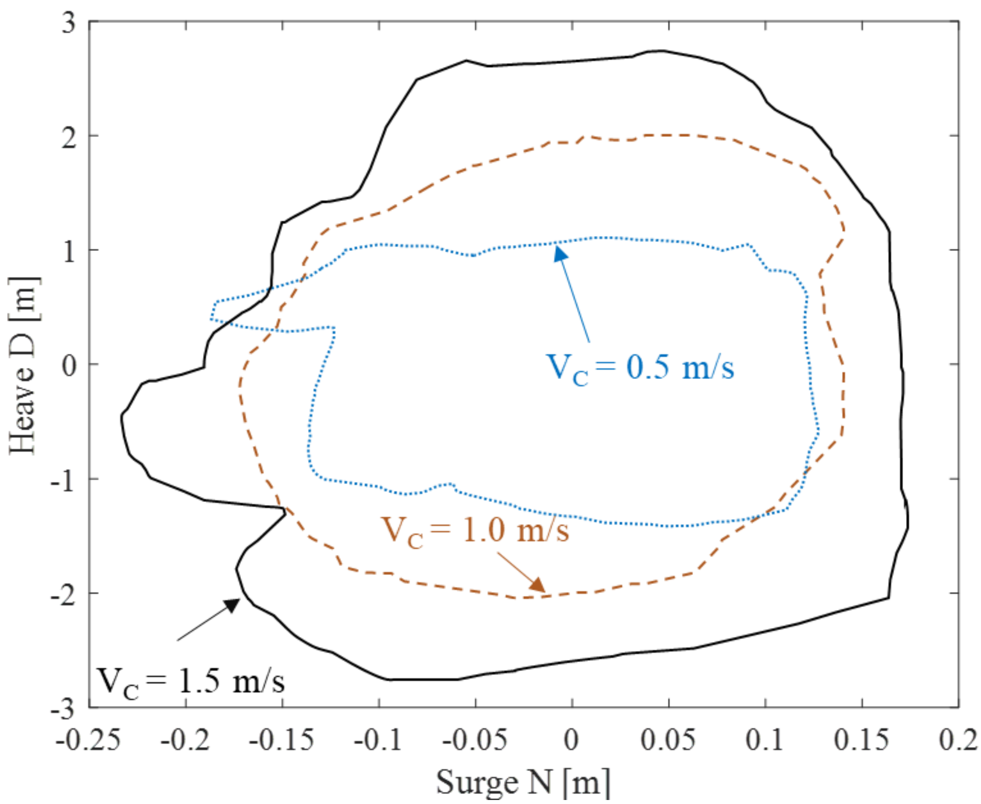

Fig. 12 Observed trajectory envelope of the SST for four hours

Finally, the trajectory envelope of the SST is summarised as Fig. 12. It is an outline of the footprint of SST of the four-hour simulations. The envelope's area expands with the increasing mean current speed. The heave offset is 1 m, 2 m, and 2.5 m for 0.5 m/s, 1 m/s, and 1.5 m/s current speeds, respectively. The surge motions are insignificant compared to heave. The maximum surge offset is -0.25 m for 1.5 m/s current speed case. As the SST has a 164 m length and 17 m beam, the motions of the presented cases are small. Therefore, the SST is stable during the entire offloading process.

5 CONCLUSIONS AND FUTURE WORKS

An SST manoeuvring model is proposed and an LQR controller is designed for hovering stability in this paper. First, a planar model is developed based on the baseline design geometry to study the SST's vertical position keeping current using its propeller and two independent tunnel thrusters. The ocean current profile follows a first-order Gauss-Markov process. SST motions are first measured by a Luenberger observer and then delivered to an LQR to calculate the control input. Four linearisation points are studied to obtain the SST linear state-space model. The results show that although the selection of linearisation points will not affect the stability of the closed-loop system, a 1 ° smaller inflow angle can lead to better controller gain performance. However, the inflow angle cannot be reduced to 0 ° as the thruster contributions are not captured. The controllability and observability of the linearised SST state-space model are confirmed. The Luenberger observer can provide good measurement to SST states. However, better observation is found on heave motion than surge and pitch motions. Moreover, placing the observer poles further to the negative real axis can reduce this error and increase hovering performance.

The scope of this work is to develop a model to describe the SST station-keeping problem that can help the design and operation of the SST vessel and its relevant facilities. Case studies of three four-hour time-domain simulations confirmed that the SST could keep its position using its equipped actuators. Sufficient thrust can be provided from tunnel thrusters to cope with 1 m/s designed current speed. Finally, an envelope of SST trajectory during offloading under three different mean current velocities is outlined.

SST's maximum heave and surge motions grow with the current speed. The maximum surge and heave motions are 0.25 m and 2.5 m for 1.5 m/s extreme current velocity.

The model developed in this paper will serve as a basis to answer critical questions regards to the design and operation of the SST and infrastructures related to it. Further, it can help improve the understanding of manoeuvring and the development of extra-large autonomous subsea vessels.

In addition, the following research studies are undergoing and planned using the model developed in this work:

- Functionality failure study: a functionality issue may be caused by system failure or extreme current speed, this can further cause a loss of structural integrity, i.e., collision or exceeding collapse depth. The developed model can be used to study the failure conditions such as single tunnel thruster malfunction.
- Extreme loading conditions: knowing the extreme response of the SST is vital not only for the design but also for the operation of the SST. A probabilistic method can be used to predict the maximum response during hovering. This can be used to knock down the designed collapse pressure for the pressure hull and identify the safety distance of the SST from the surface or subsea installations.
- Flowline design: this model will be further coupled with dynamic tools like SIMA or OrcaFlex for offloading subsea flowline design.

COPYRIGHT REMINDER

The authors declare no known conflicts in the copyrights. All figures and tables used in the article are from the authors’ original work.

ACKNOWLEDGMENT

The authors declare no known conflict of interest.

FUNDING

The authors declare no funding resources for this work.

REFERENCES

[1] Norsk Petroleum, 2021, "The oil and gas pipeline system," https://www.norskpetroleum.no/en/production-and-exports/the-oil-and-gas-pipeline-system/.

[2] Kenny, S., 2018, "Offshore pipelines—Elements of managing risk," Methods in Chemical Process Safety, F. Khan, and R. Abbassi, eds., Elsevier, pp. 289-325.

[3] Xing, Y., "A conceptual large autonomous subsea freight-glider for liquid CO2 transportation," *Proc. ASME 2021 40th International Conference on Ocean, Offshore and Arctic Engineering*. DOI: 10.1115/omae2021-61924

[4] Ma, Y., Xing, Y., Ong, M. C., and Hemmingsen, T. H., 2021, "Baseline design of a subsea shuttle tanker system for liquid carbon dioxide transportation," Ocean Engineering, **240**. DOI: 10.1016/j.oceaneng.2021.109891

[5] Jacobsen, L. R., "Subsea transport of arctic oil - a technical and economic evaluation," *Proc. Offshore Technology Conference*Dallas, Texas. DOI: 10.4043/1425-MS

[6] Moloney, M. P., 1974, "Submarine tanker concepts and problems," National Maritime Research Center.

[7] Taylor, P. K., and Montgomery, J. B., "Arctic submarine tanker system " *Proc. Offshore Technology Conference*Houston, Texas. DOI: 10.4043/2998-MS

[8] Jacobsen, L., Lawrence, K., Hall, K., Canning, P., and Gardner, E., 1983, "Transportation of LNG from the arctic by commercial submarine," Marine Technology and SNAME News, **20**(04), pp. 377-384. DOI: 10.5957/mt1.1983.20.4.377

[9] Jacobsen, L. R., and Murphy, J. J., 1983, "Submarine transportation of hydrocarbons from the arctic," Cold Regions Science and Technology, **7**, pp. 273-283. DOI: 10.1016/0165-232X(83)90073-3

[10] Equinor Energy AS, 2019, "RD 662093-Subsea shuttle system," Research Disclosure

[11] Ellingsen, K. E., Ravndal, O., Reinås, L., Hansen, J. H., Marra, F., Myhre, E., Dupuy, P. M., and Sveberg, K., 2020, "RD 677082-Subsea shuttle system," Research Disclosure

[12] Xing, Y., Ong, M. C., Hemmingsen, T., Ellingsen, K. E., and Reinås, L., 2021, "Design considerations of a subsea shuttle tanker system for liquid carbon dioxide transportation," Journal of Offshore Mechanics and Arctic Engineering, **143**(4). DOI: 10.1115/1.4048926

[13] Xing, Y., Santoso, T. A. D., and Ma, Y., 2021, "Technical–economic feasibility analysis of subsea shuttle tanker," Journal of Marine Science and Engineering, **10**(1), p. 20. DOI: 10.3390/jmse10010020

[14] Anderson, B. D. O., and Moore, J. B., 2007, Optimal Control: Linear Quadratic Methods, Dover Publications, Inc., Mineola, New York.

[15] Fossen, T. I., 2011, Handbook of Marine Craft Hydrodynamics and Motion Control, John Willey & Sons, Ltd, West Sussex, UK.

[16] Mendes, C. H., Bentes, C., Rebelo, T. A., and Bousson, K., "Guidance and robust control of a double-hull autonomous underwater vehicle," *Proc. ICEUBI2017 - International Congress on Engineering 2017*, Universidade da Beira Interior, pp. 1194-1203

[17] Tiwari, B. K., and Sharma, R., 2020, "Design and analysis of a variable buoyancy system for efficient hovering control of underwater vehicles with state feedback controller," Journal of Marine Science and Engineering, **8**(4), p. 263. DOI: 10.3390/jmse8040263

[18] Bowers, A. H., Murillo, O. J., Jensen, R., Eslinger, B., and Gelzer, C., 2016, "On wings of the minimum induced drag: spanload implications for aircraft and birds," NASA, Edwards, California.

[19] Kongsberg, 2019, "Marine Products and Systems," https://www.kongsberg.com/globalassets/maritime/km-products/documents/product-catalog-2019.pdf.

[20] Sørensen, A. J., 2018, Marine Cybernetics (Lecture Notes), Department of Marine Technology, NTNU, Trondheim.

[21] Bruserud, K., and Haver, S., 2018, "Current conditions in the northern North Sea," Ocean Engineering, **156**, pp. 318-332. DOI: 10.1016/j.oceaneng.2018.03.025

[22] Ersdal, G., 2001, "An Overview of Ocean Currents with Emphasis on Currents on the Norwegian Continental Shelf," Norwegian Petroleum Directorate.

[23] Chen, C.-T., 1999, Linear System Theory and Control, Oxford University Press, New York.

[24] Davis, J. H., 2002, Foundations of Deterministic and Stochastic Control, Springer, Boston, MA, USA

[25] Mariano, A. J., Ryan, E. H., Perkins, B. D., and Smithers, S., 1995, "The Mariano Global Surface Velocity Analysis 1.0," United States Coast Guard Research and Development Centre, Washington DC, USA.

[26] Sætre, R., 2007, The Norwegian Costal Current: Oceaography and Climate, Fagbokforlaget Bergen, Norway.

Figure Captions List

Table Caption List